Cryogenic-temperature electron microscopy direct imaging of carbon nanotubes and graphene solutions in superacids

Article *in* Journal of Microscopy · March 2015

DOI: 10.1111/jmi.12243 · Source: PubMed

10 authors, including:

Olga Kleinerman
Technion - Israel Institute of Technology
6 PUBLICATIONS **199** CITATIONS
SEE PROFILE

Ellina Kesselman
Technion - Israel Institute of Technology
86 PUBLICATIONS **2,406** CITATIONS
SEE PROFILE

Yachin Cohen
Technion - Israel Institute of Technology
103 PUBLICATIONS **3,101** CITATIONS
SEE PROFILE

Matteo Pasquali
Rice University
231 PUBLICATIONS **5,623** CITATIONS
SEE PROFILE

Journal of Microscopy

Journal of Microscopy, Vol. 259, Issue 1 2015, pp. 16–25
Received 2 November 2014; accepted 7 February 2015

doi: 10.1111/jmi.12243

Cryogenic-temperature electron microscopy direct imaging of carbon nanotubes and graphene solutions in superacids

O. KLEINERMAN*, A. NICHOLAS G. PARRA-VASQUEZ†, M.J. GREEN†,‡, N. BEHABTU†, J. SCHMIDT*, E. KESSELMAN*, C.C. YOUNG†, Y. COHEN*, M. PASQUALI†,§,‖ & Y. TALMON*

**Department of Chemical Engineering and the Russell Berrie Nanotechnology Institute, Technion—Israel Institute of Technology, Haifa, Israel*

†The Richard E. Smalley Institute for Nanoscale Science and Technology, Rice University, Houston, Texas, U.S.A.

‡Artie McFerrin Department of Chemical Engineering, Texas A&M University, College Station, Texas, U.S.A.

§Department of Chemical & Biomolecular Engineering and Chemistry, Rice University, Houston, Texas, U.S.A.

‖Department of Materials Science & NanoEngineering, Rice University, Houston, Texas, U.S.A.

Key words. Carbon nanotubes, controlled environment vitrification system, cryo-SEM, cryo-TEM, specimen preparation, superacid.

Summary

Cryogenic electron microscopy (cryo-EM) is a powerful tool for imaging liquid and semiliquid systems. While cryogenic transmission electron microscopy (cryo-TEM) is a standard technique in many fields, cryogenic scanning electron microscopy (cryo-SEM) is still not that widely used and is far less developed. The vast majority of systems under investigation by cryo-EM involve either water or organic components. In this paper, we introduce the use of novel cryo-TEM and cryo-SEM specimen preparation and imaging methodologies, suitable for highly acidic and very reactive systems. Both preserve the native nanostructure in the system, while not harming the expensive equipment or the user. We present examples of direct imaging of single-walled, multiwalled carbon nanotubes and graphene, dissolved in chlorosulfonic acid and oleum. Moreover, we demonstrate the ability of these new cryo-TEM and cryo-SEM methodologies to follow phase transitions in carbon nanotube (CNT)/superacid systems, starting from dilute solutions up to the concentrated nematic liquid-crystalline CNT phases, used as the 'dope' for all-carbon-fibre spinning. Originally developed for direct imaging of CNTs and graphene dissolution and self-assembly in superacids, these methodologies can be implemented for a variety of highly acidic systems, paving a way for a new field of nonaqueous cryogenic electron microscopy.

Introduction

To image nanoscale domains in a liquid requires either transmission electron microscopy (TEM) or scanning electron microscopy (SEM). These are the only techniques that provide the resolution needed for imaging nanometric details. Yet, imaging these systems in the high vacuum of electron microscopes is challenging, because liquids have considerable vapour pressure. Moreover, to attain proper resolution, samples should be free of motion (e.g., Brownian motion). The specimen must be sufficiently thin for TEM, and not charge in SEM. The specimens must offer sufficient contrast, namely, that domains of different composition, e.g., oil and water domains or suspended aggregates and the liquid phase, interact differently with the electron beam. Yet another difficulty of electron microscopy of 'soft matter' systems is their high sensitivity to electron radiation-damage, namely destruction of the examined specimen by the electron beam, even at very short electron exposures (Talmon *et al.*, 1986).

Cryogenic-temperature transmission electron microscopy (cryo-TEM) is now the *de facto* standard tool in the study of complex liquids, particularly so when liquid systems comprises nanoscale colloids such as nanoparticles, surfactants, viruses, or vesicles and micelles (Friedrich *et al.*, 2010). Methodologies have been developed to capture the nanostructures of liquid systems, while preserving their original state at a given concentration and temperature (Bellare *et al.*, 1988; Frederik & Hubert, 2005). Cryo-TEM is now widely used to study synthetic, biological and medical systems. Originally developed for aqueous systems, it has been also applied successfully in the study of nonaqueous systems (Kesselman *et al.*, 2005; Bang *et al.*, 2006; Dudkiewicz *et al.*, 2011). However, this methodology cannot be used to study highly viscous systems, or those containing objects larger than several hundreds of nanometres (Talmon, 2007).

Recent developments have made high-resolution scanning electron microscopy (HR-SEM) ideal for imaging nanoparticles and colloids in viscous systems as well as nanoscale features in

Correspondence to: Y. Talmon, Department of Chemical Engineering, Technion—Israel Institute of Technology, Haifa 32000, Israel. Tel: +972-4-8292007; e-mail: ishi@tx.technion.ac.il

systems containing large objects, hundreds of nanometres and larger. Improved field-emission electron guns, electron optics and detectors have enabled imaging nanoparticles down to a few nanometres (Pohl & Jaksch, 1995; Jaksch *et al.*, 2003). Liquid nanostructured systems can now be studied by cryo-SEM using much-improved cryogenic specimen holders and transfer systems (Wepf *et al.*, 2004). In recent years, we have developed a novel specimen preparation methodology for cryo-SEM specimens that preserves the original nanostructure of labile complex liquids at specified composition and temperature, quite similarly to what had been done in cryo-TEM (Issman & Talmon, 2012).

Cryo-EM involves rapid cooling of the specimen by plunging into a suitable cryogen. Because many of the nanostructured liquid systems studied by cryo-EM are sensitive to small changes of temperature and concentration, specimen preparation prior to plunging must be carried out in a closed chamber, where the temperature and saturation of the gas phase are kept constant. The controlled environment vitrification system (CEVS) was originally designed for preparing cryo-TEM specimens (Bellare *et al.*, 1988) and recently modified for cryo-SEM specimen preparation (Issman & Talmon, 2012). Commercial CEVS-type systems, such as the FEI 'Vitrobot' and the Leica 'EM GP', can be used for preparing cryo-TEM specimens of aqueous system only.

Another class of cryo-EM techniques is freeze–fracture–replication (Steere, 1957 (the original paper describing the technique); Omer *et al.*, 2009 [a recent application for a non-biological problem)]. It involves fast cooling of the liquid specimen, fracturing it, and the preparation of a metal–carbon replica of the fracture surface. The specimen is removed, and the replica is retrieved, cleaned and imaged at room temperature in the TEM. In addition to plunge-cooling, 'jet freezing' (Moor *et al.*, 1976; Mueller *et al.*, 1980) and 'high pressure freezing' (Moor & Riehle, 1968) are also often used to achieve higher cooling rates.

In this paper, we describe the application of cryo-EM to the study of liquid systems containing superacids, such as fuming sulfuric acid (oleum, with up to 30% excess SO_3) and, especially, chlorosulfonic acid (CSA). These systems are difficult to handle because CSA is highly hygroscopic and a strong oxidant; yet, their imaging became imperative because these acids are the only true solvents for carbon nanotubes (CNTs) and graphene sheets (Ramesh *et al.*, 2004; Davis *et al.*, 2009; Behabtu *et al.*, 2010). Using the methodologies we describe below (with examples of applications), high-resolution cryo-TEM of low-concentration CNTs or graphene solutions in superacids was used to prove conclusively dispersion at the molecular level. Cryo-SEM of high-concentration CNT liquid crystals is being investigated to study spontaneous CNT ordering in dopes used for spinning carbon fibres of extremely high mechanical strength and electrical and thermal conductivity (Behabtu *et al.*, 2013).

Experimental details

Materials

We studied several types of single-walled nanotubes (SWNTs), double-walled nanotubes (DWNTs), multiwalled nanotubes (MWNTs) and graphene, produced by various manufacturers by different methods. HiPco and carpet-grown SWNTs (Pint *et al.*, 2008) were produced at Rice University, DWNTs were obtained from CCNI (Continental Carbon Nanotechnologies Inc., XBC grade, Houstan, TX, U.S.A.). CVD-grown Sunnano MWNTs were obtained from Sun Innovations, Inc. (Fremont, CA, U.S.A.). Highly ordered pyrolytic graphite (HOPG), was obtained from SPI Supplies (West Chester, PA, U.S.A.).

ACS-certified CSA (density: 1753 kg m^{-3}) and oleum (20 wt.% excess SO_3; density: 1925 kg m^{-3}) were used as received from Sigma-Aldrich (St. Louis, MO, U.S.A.). The chemicals were stored in a glove-box, with a continuous flow of dry air.

Solution preparation

CNTs and graphene were dispersed in CSA. HiPco SWNTs were also dispersed in oleum (fuming sulfuric acid, with 20 wt.% excess SO_3). Preparation and further storage of the solutions were carried out in a glove-box, continuously purged with dry air. All vials were sealed with Teflon tape. To achieve homogeneous dispersion, the diluted solutions were mixed with a stir-bar for a day. A SpeedMixer (Haushild Eng., Germany) was used for mixing viscous solutions of higher content of carbon nanotubes. From cryo-EM experiments, we have found that there is a strong effect of solution age on CNT aggregation (Davis *et al.*, 2009) due to slow acid degradation with time. In this work, we used only freshly made samples.

Cryo-TEM specimen preparation

For cryo-specimen preparation, a small drop (ca. 3 μL) of sample solution was applied on a perforated carbon film supported on a copper TEM grid (lacey Formvar/carbon films on 200 mesh Cu grids, from Ted Pella, Redding, CA, U.S.A.), held by tweezers inside a CEVS (Bellare *et al.*, 1988), covered with a flexible polyethylene "glove-bag" (Sigma-Aldrich). To achieve good wettability of the support, the perforated films were cleaned with glow discharge air-plasma (PELCO easiGlow™, Ted Pella Inc., Redding, CA, U.S.A.). The CEVS was kept at 25 °C with continuous purging of pure dry nitrogen gas, preventing the ingress of moisture. To avoid interactions between superacid and organic material, glass fibre filter paper (instead of cellulose filter-paper) was used for blotting samples into thin films, followed by plunging into boiling liquid nitrogen (instead of liquid ethane at its freezing point, the

cryogen of choice in cryo-TEM). Although boiling liquid nitrogen yields slower cooling rates than liquid ethane at its freezing point (Siegel *et al.*, 1994), it does vitrify CSA and oleum.

The speed of sample preparation plays an important role. Once the drop is placed onto the grid and blotted, the grid must be plunged quickly into the cryogen to preserve the original nanostructures, because CSA can otherwise react with the copper grid, leading to CNT agglomeration and contamination of the sample by copper compounds. CSA may also react with the support film.

Some of the specimens were examined in a Philips CM120 TEM at an accelerating voltage of 120 kV. An Oxford CT3500 cryo-specimen holder was used to maintain the vitrified specimens below –175°C in the TEM. Other specimens were examined in an FEI Tecnai 12 G^2 TEM using a Gatan 626 cryo-holder. Specimens were studied in the low-dose imaging mode to minimize electron beam exposure and radiation damage. Images were recorded digitally by a Gatan MultiScan 791 cooled CCD camera (Philips microscope), or by a high-resolution 2k × 2k Gatan US1000 cooled CCD camera, using the Digital Micrograph software (Gatan, U.K.).

After imaging, the cryo-holder is taken out of the microscope and its tip is dipped in a large beaker of distilled water to neutralize the small volume of acid in the specimen. Taking this precaution prevents any damage to the microscope or the specimen holder from the specimen.

Cryo-SEM specimen preparation

Cryo-SEM can image bulk material, hundreds of micrometres in thickness. A number of techniques are used to vitrify specimens for cryo-SEM (Moor & Riehle, 1968; Moor *et al.*, 1976; Knoll *et al.*, 1982; Hisada *et al.*, 2001). However, these methodologies do not control the sample environment during cryo-specimen preparation, prior to thermal fixation. This drawback makes them ineffective for handling reactive liquids, such as CSA and other superacids.

To allow direct imaging of viscous solutions, containing high concentrations of CNTs in CSA, we have developed a novel technique, based on the controlled sample preparation procedure, recently described in detail by Issman & Talmon (2012), which include steps described earlier by Omer *et al.* (2009).

Cryo-specimen preparation is carried out in a CEVS, covered with a flexible polyethylene "glove-bag" and continuously purged with dry N_2 gas. A drop of sample solution is applied between two gold planchettes. To improve the adhesion of the solution to the substrate, the planchettes are treated with glow-discharge air-plasma just before the experiment. The sample is loaded on custom designed tweezers (Issman & Talmon, 2012) and plunged into LN_2 at its boiling point. The sandwich with vitrified solution is inserted into a special Leica 'sample-table', cooled in LN_2. Further treatment includes fracturing the vitrified sample and optional coating with 4 nm of conductive layer of Pt/C at 90° to the fractured surface. Fracturing and coating are performed in a BAF060 unit (Leica, Liechtenstein) precooled to –170°C, kept under high vacuum ($\sim 2\times10^{-4}$ Pa). We do not attempt to improve surface topography contrast by acid sublimation, because of the low vapour pressure of the acid and its potential corrosive vapour.

Fractured cryo-specimens are transferred to a Zeiss Ultra Plus HR-SEM by pumped and precooled VCT-l00 shuttle (Leica, Liechtenstein). The microscope is equipped with Leica VCT-100 cold-stage maintained at –145°C for cryo-high-resolution SEM imaging. The specimens are examined at very low electron acceleration voltage (0.7–1 kV) and short working distance (2.9–3.3 mm), optimal conditions for high-resolution imaging. Both the in-the column ('InLens' in the jargon of Zeiss) and the Everhart-Thornley ('SE2') secondary electron imaging detectors were used in this study. The images were digitally recorded by the Zeiss Ultra Plus software and analysed by the CS5 Photoshop software.

As with cryo-TEM, after imaging the cryo-holder ('specimen table') is taken out of the microscope and is dipped into a large beaker of distilled water to neutralize the small volume of acid in the specimen. That prevents any damage to the microscope or the 'specimen-table' from the specimen.

Cryo-TEM imaging

Contrast. In TEM, both amplitude and phase contrast mechanisms contribute to image formation. Amplitude contrast is related to scattering/absorbing by the atoms in observed area, which depend strongly on the atomic number, as well as on the local thickness of the specimen (mass–thickness contrast). Phase contrast, however, arises from the interference of scattered and transmitted beams and is controlled by defocusing objective lens (Egerton, 2005). For cryo-TEM imaging, we use the low-dose mode to minimize electron beam radiation damage, typically keeping electron exposure below 20 e^- $Å^{-2}$.

CSA and sulfuric acid have high electron density because of the presence of sulfur and chlorine atoms. Thus, the vitrified acid matrix is more optically dense than the CNTs or graphene embedded in it and appears darker than the dispersed objects. However, the relatively large thickness of the vitrified acid matrix in comparison to nanometre-scale thickness of the embedded aggregates (especially SWNTs), together with the spontaneous filling of nanotubes by the acid (Green *et al.*, 2011), reduces the contrast dramatically. We have found that controlling the cryo-specimen and imaging parameters, such as film thickness, electron exposure and underfocus, are critical for good contrast.

Contrast enhancement by selective electron-beam radiation damage. Due to the poor inherent mass–thickness contrast in superacid systems, contrast enhancement by controlled electron beam irradiation damage of cryo-specimens plays an important role in imaging such systems. Moreover, as film

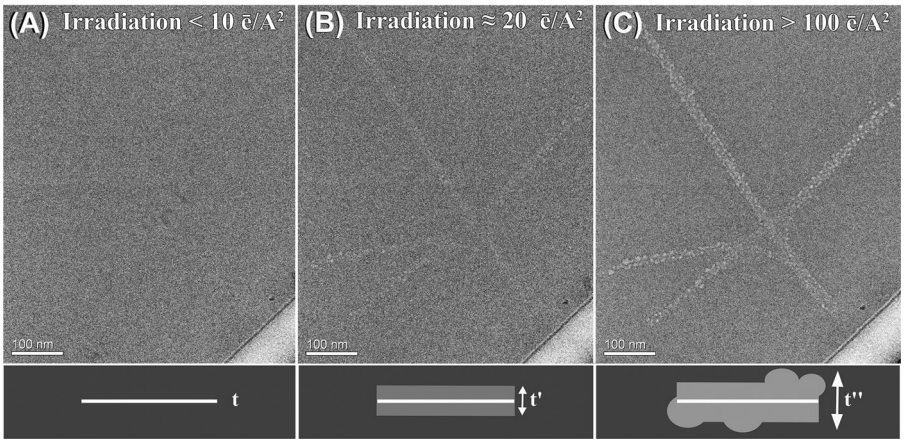

Fig. 1. Effect of electron exposure on a cryo-specimen of short SWNTs. (A) Initial exposure below 10 e^{-} Å^{-2}, showing no structure. (B) Cumulative exposure of 20 e^{-} Å^{-2}, with visible SWNTs, as some surrounding CSA is removed. (C) Additional irradiation above 100 e^{-} Å^{-2} leads to formation of larger cavities around the SWNTs. The brighter lower right corner is a segment of the perforated carbon support film. The frames below the images are schematic cross-sections of the specimens, showing the etching of the acid around the SWNT as function of electron exposure. Grey areas are cavities formed by loss of acid.

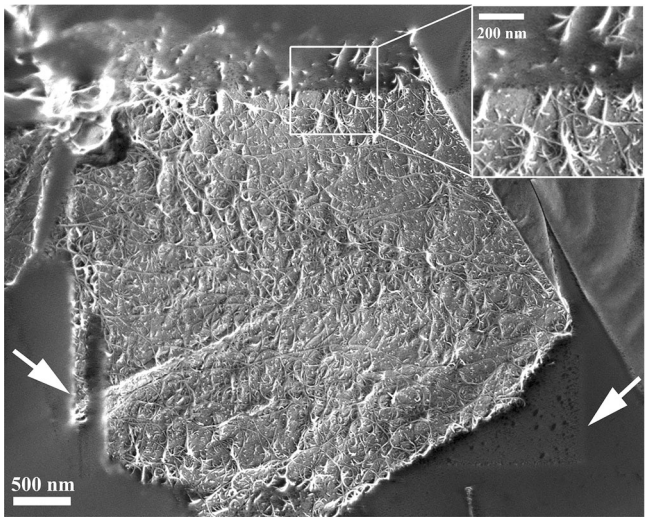

Fig. 2. Contrast enhancement during cryo-SEM imaging of HiPco SWNTs in CSA. A layer of CSA prevents imaging of SWNTs. After exposing the same area to the e-beam for 3 min at same imaging conditions (cumulative e-dose ≈ 150 e^{-} Å^{-2}), a thin layer of acid was etched away, revealing the SWNT morphology. White arrows point on the etching boundaries. The inset is an enlarged part of the micrograph showing very clear the boundary between the area that received minimal beam interaction (upper part) and the area after 3 min of exposure to the electron beam (lower part).

thickness increases, controlled irradiation of the film by e-beam is the only way to reveal the carbon nanostructures embedded in the vitrified acid matrix. The mechanism of radiation damage is not fully understood yet. Most likely, the electron beam creates free radicals, H·, OH·, SO_4·, SO_3· and SO_2· in the sulfur acid (Henriksen & Jones, 1971). In CSA, Cl· radicals may also be formed. In vitrified specimens of organic aggregates in water-containing media, the free radicals formed by splitting water attack organic material at the water–organic interface (Mortensen & Talmon, 1995; Yan *et al.*, 2007), giving rise to enhanced contrast. Similarly, we suggest that free radicals are more rapidly formed at the CNT surface, leading to faster mass loss from the acid there, forming narrow cavities around the CNTs, thus enhancing mass–thickness contrast.

To demonstrate contrast enhancement by electron irradiation, we recorded a series of images at increasing electron exposures (Fig. 1). Figure 1(A) was recorded with less than 10 e^{-} Å^{-2}; the SWNTs are not visible because of the very low mass–thickness contrast. The image consists of a dark area (acid) with a brighter lower right corner (a segment of the perforated carbon). By increasing the electron exposure to 20 e^{-} Å^{-2}, lighter areas of CNTs in the vitrified acid became visible (Fig. 1B). Further irradiation of the same area to a total exposure of more than 100 e^{-} Å^{-2}, led to the formation of bubble-like cavities around the SWNTs, giving additional contrast enhancement (Fig. 1C).

By adjusting the electron dose to the thickness of the vitrified acid cryo-specimens (thicker areas require more etching), one can generate sufficient contrast to image carbon nanotubes and graphene in superacids (Davis *et al.*, 2009; Behabtu *et al.*, 2010; Parra-Vasquez *et al.*, 2010; Green *et al.*, 2011; Behabtu, 2012) We have used irradiation contrast enhancement in the development of a method for measuring the length of individual CNTs (Bengio *et al.*, 2014).

Cryo-SEM imaging

Image formation in SEM is affected by many factors: acceleration voltage of the primary electrons, type and location of the detector and nature of the specimen: composition, electrical conductivity and topography. Cryo-SEM imaging is complicated by enhanced electrical charging (mainly because of

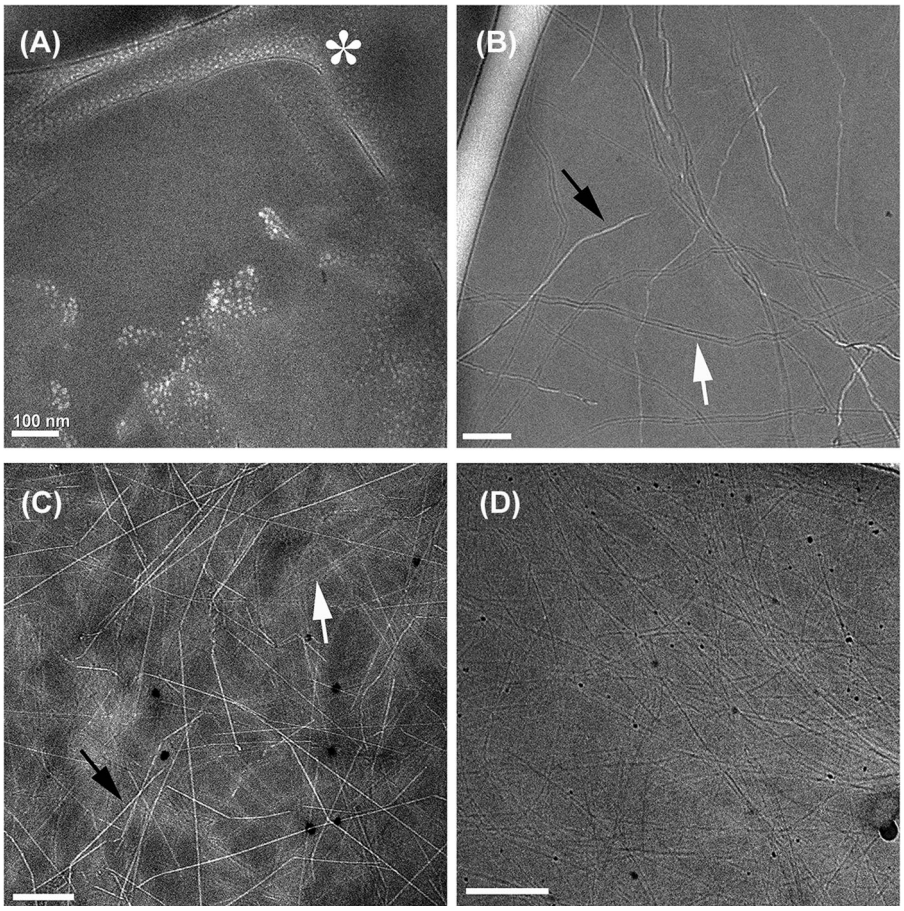

Fig. 3. Cryo-TEM images of graphene or CNTs in CSA: (A) Graphene flakes dispersed CSA. There is poor mass–thickness contrast between the lacey carbon (asterisk) and the acid, indicating a relatively thick specimen. The acid was preferentially etched by electron beam dose of about 70 e^{-} $Å^{-2}$, enhancing the contrast. (B) 50 ppm (wt.) Sunnano MWNTs dispersed in CSA. (C) 100 ppm (wt.) isotropic solution of carpet-grown SWNTs in CSA. In (B) and (C) note hollow and acid-filled MWNTs (black and white arrows, respectively). (D) 1500 ppm (wt.) isotropic solution of purified HiPco SWNTs (average diameter of 1–2 nm) in CSA. These nanotubes appear as dark threads over the slightly etched acid. Black spots are remaining catalyst particles. Bars = 100 nm.

nonuniform adhesion of cryo-specimens to the substrate and poor conductivity of some liquid systems) and by electron-beam radiation damage. In secondary electron imaging, contrast of CNTs in CSA is mostly topographic contrast, although some contrast may arise from differential charging in areas of high concentration of CNTs due to their electrical conductivity. In the backscattering electron imaging mode, one can obtain elemental contrast between the CNTs and the acid. In most cases, we did not use any metal or carbon coating. To avoid electrical charging of the specimens, we used short dwell times per pixel (100 ns $pixel^{-1}$), compensating for the weak signal by scanning each picture line at least ten times, and averaging, which allowed local charging to dissipate, before the same pixel was hit again by the beam. We always use electron accelerating voltage corresponding to the point of neutrality, namely when the number of electrons emitted from the specimen is equal to the number of electrons hitting it (Plies, 1994; Goldstein *et al.*, 2003). At those conditions, even non-conducting specimens do not charge electrically, even without a conductive coating. For many materials, including vitrified CSA specimens, this occurs at electron acceleration voltage around 1 kV, which is the accelerating voltage we used.

As noted above, the accelerated electrons interact with the vitrified superacid in a free-radical reaction, which propagates at a higher rate at the CNT–acid interface. The probability of ionization events depends inversely on acceleration voltage (Goldstein *et al.*, 2003). Therefore, in cryo-SEM, when using typical electron acceleration voltage of ~1 kV, we observe much higher rate of acid loss during imaging than in cryo-TEM (120 kV). This mass loss ('etching') could be used to expose CNTs, originally embedded in the vitrified acid (not necessarily exposed by fracturing the specimen) and thus enhance topographic contrast in secondary electron imaging of the cryo-SEM specimen, as shown in Figure 2.

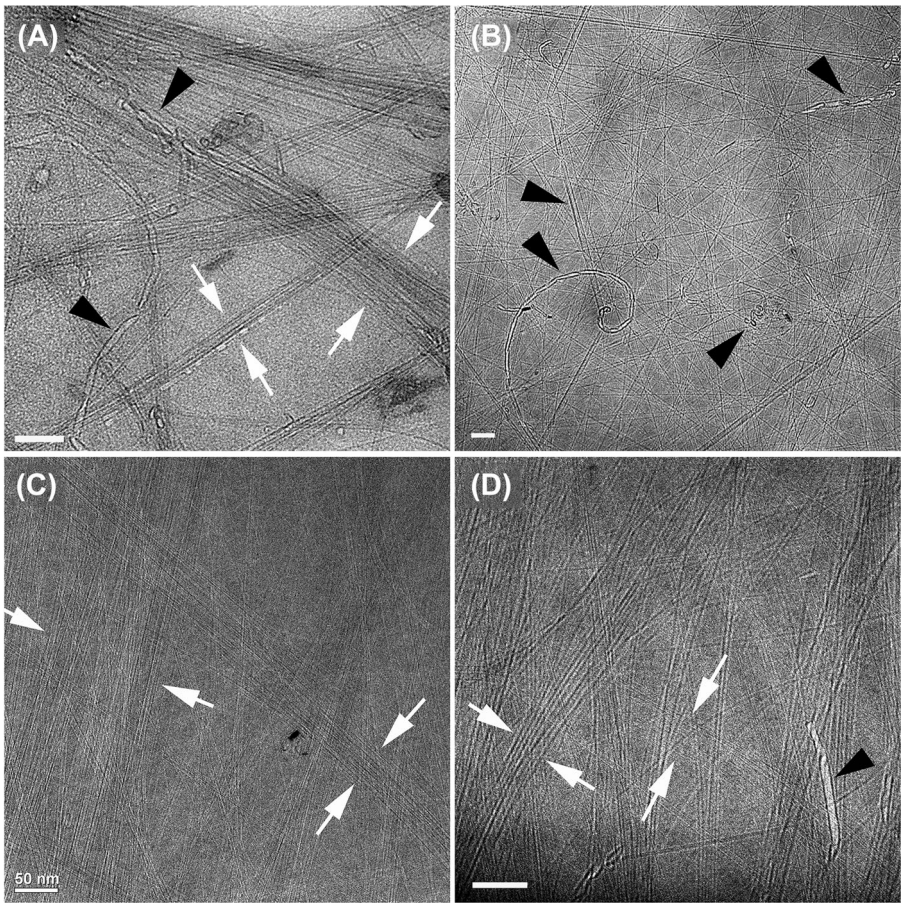

Fig. 4. Cryogenic-TEM images of liquid crystalline phase development in CNTs in CSA solutions. (A) Liquid crystalline phase formation in a solution of 570 ppm (wt.) CCNI XBC 1002 SWNTs in CSA. 15–50-nm wide nanobundles are observed, indicating the beginning of aligned phase formation (white arrows). Distorted MWNTs are seen as well (black arrowheads), coming out of the aligned phase. (B) An isotropic region in the same specimen as (A). A wide distribution of nanotube diameter and quality is observed (black arrowheads). (C) and (D) show a network of aligned CNT bundles in the biphasic region. (C) 1000 ppm (wt.) CCNI XBC 1002 DWNTs in CSA and (D) 1000 ppm (wt.) CCNI XBC 1001 DWNTs in CSA. The bundles consist of molecules with similar diameter (white arrows), while the impurities are segregated out of the aligned phase (black arrowheads). Bars = 50 nm.

Methodology applications and discussion

The micrographs in Figure 3 demonstrate some typical features of cryo-TEM of graphene and CNTs in vitrified CSA. Figure 3(A) shows graphene flakes dispersed in CSA. This is a rather thick specimen that has very little contrast between the graphene and acid. Electron beam irradiation, which formed small holes (lighter round domains) at the interface between the acid and the carbon support film (denoted with an asterisk) and the graphene (lower part of the micrograph), enhanced the contrast. More details are given by Behabtu *et al.* (2010). Figure 3(B) shows a much thinner area of a vitrified specimen of MWNTs in CSA. Even with minimal e-beam irradiation there is good contrast between the perforated carbon support film (light area, upper left) and the acid.

Spontaneous CNT filling with liquids (for example Gogotsi *et al.*, 2002; Bekou & Mattia, 2011) and with CSA in particular (Green *et al.*, 2011) was recently observed by cryo-TEM and other techniques. Big diameter MWNTs all are readily discernible due to the thinness of the vitrified specimen (Fig. 3B). Acid-filled SWNTs are denoted by a white arrow, and empty SWNTs by a black one (Figs. 3B,C). In some cases, the imaged SWNTs appear darker than exposed acid (Fig. 3D). CNT filling could be directly related to defects along CNT walls or to open end-caps. No detailed study on the mechanism of CSA uptake by nanotubes has been performed. However, our impression is that once a CNT is damaged, it is filled with the acid, regardless of its diameter.

In systems of stiff rods [described by Onsager and Flory classical theories (Onsager, 1949; Flory, 1956)], at low concentration, the rods do not interact and diffuse freely. As the rod concentration grows, first the rotational diffusion slows down (semidilute regime), and then, the translational diffusivity is impacted (concentrated regime), while the orientation of the rods remains isotropic. Increasing the concentration further forces the system to phase-separate into a liquid crystalline

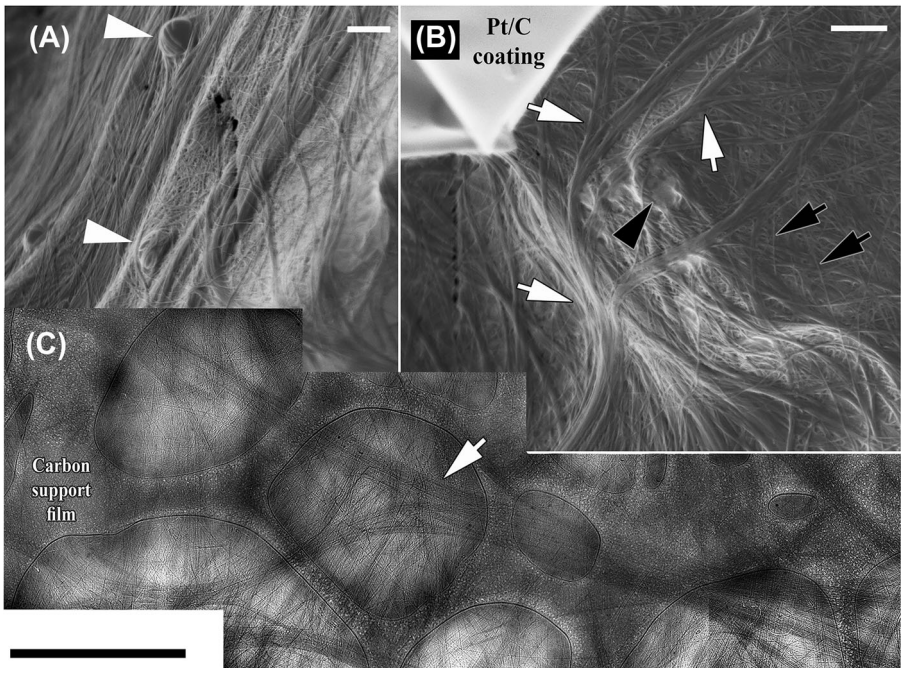

Fig. 5. (A) and (B) cryo-SEM images showing biphasic regions of CNTs in CSA bulk solutions (0.5 wt.% CCNI XBC 1001 DWNT in CSA). SiO_2 microparticles (white arrowheads) were used to promote cryo-specimen fracture. The structures are exposed by gentle e-beam etching of uncoated areas. Residual (nonetched) acid layer, covering the structures is recognizable (black arrowhead). Black arrows point on individual CNTs in isotropic phase, and white arrows point on CNT aligned bundles. CNT arrangement in solution observed by cryo-SEM is in agreement with (C) cryo-TEM observations of 0.25 wt.% CCNI XBC 1001 DWNT in CSA, showing CNT arrangement into aligned domains (white arrow). The image (C) is stitched of five micrographs. Bars = 500 nm.

(ordered) phase in equilibrium with an isotropic concentrated phase and, eventually, to the formation of single liquid crystalline phase at a sufficiently high concentration. Phase transition concentration varies with solvent and solute parameters as well as any length polydispersity of the rods (Flory & Abe, 1978). However, on the macroscopic scale, each transition yields well-defined changes in the concentration-dependent viscosity (Larson, 1999). When the system transitions to a liquid crystalline phase, the rheological behaviour becomes unique, where the viscosity drops with increasing concentration; this behaviour is well known in liquid crystalline rod-like polymers and is observed also in CNT/superacid solutions (Davis *et al.*, 2004; Green *et al.*, 2009a, 2009b). The combination of cryo-TEM and cryo-SEM imaging allowed us, for the first time, to study systematically the development of a nematic liquid crystalline phase made of CNTs in CSA, as a function of the CNT type and concentration at nanoscopic level.

Following the imaging of the isotropic phase of CNTs in CSA, we studied extensively the biphasic region, near the isotropic–biphasic boundary for long CNTs. Figure 4(A) shows ordered (aligned) phase development at its earlier stages, characterized by the formation of 15–50-nm-wide aligned domains. Considerable areas of isotropic phase are observed in the same cryo-specimen, with visible impurities and wide CNT diameter and morphology distribution (Fig. 4B). By doubling the CNT concentration, thicker CNT aligned domains are observed, coexisting with thinner one (Figs. 4C,D). This phenomenon was detected in all examined long double-walled CNTs (tens of micrometres long). Moreover, LC phase development is accompanied by the segregation of defective or "different" CNTs and impurities out of the aligned phase (black arrowheads in Figs. 4A,D). Moreover, CNTs of similar diameter appear to self-assemble into aligned domains (white arrows in Figs. 4C,D), a phenomenon we observed in all types of long CNTs.

We also studied the biphasic regions of long CNTs in bulk solution by cryo-SEM. Cryo-SEM allows imaging of viscous specimens that cannot be made into the very thin cryo-TEM specimens. Figures 5(A) and (B) show cryo-SEM images of CCNI XBC DWNTs in the biphasic regime. Aligned 'threadlike' domains of long nanotubes are clearly observed, superposed on an isotropic phase background. Individual CNTs are recognized in isotropic phase (black arrows in Fig. 5B), while the ordered phase consists of several CNTs, aligned along their long axis. Thinner domains are merged into thicker ones, forming long nematic domains (white arrowheads in Fig. 5B).

Cryo-SEM specimen preparation presented special challenges. Low CNT content in these solutions prevented the formation of well-fractured surfaces suitable for imaging.

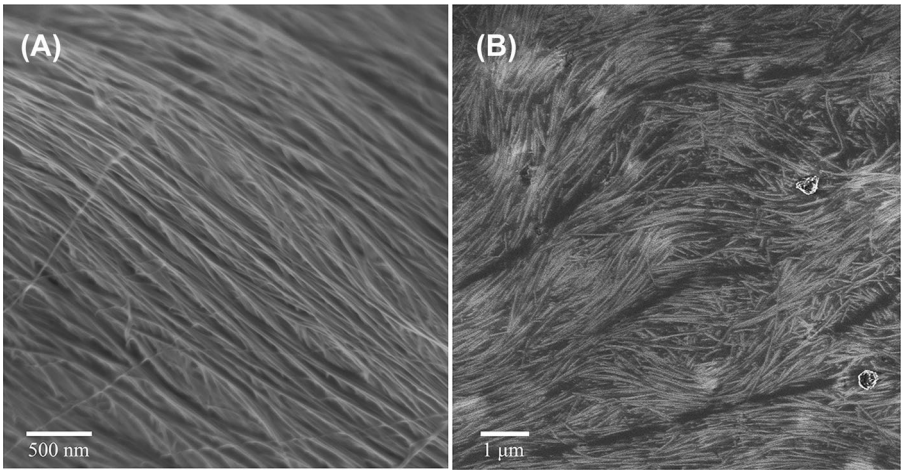

Fig. 6. Cryo-SEM images of liquid crystalline domains formed by (A) 3 wt.% CCNI XBC 1101 (mostly DWNTs) in CSA. Highly ordered, tens of micrometres long liquid crystalline domains are observed. (B) HiPco SWNTs in CSA, 6 wt.% CNTs in CSA. Narrow (up to 10 μm width) and short liquid crystalline domains are observed.

To induce fracture propagation, we added a small amount ($\sim$300 μg ml^{-1}) of SiO_2 microparticles (500 nm in diameter, Cabot Corp., Boston, MA, U.S.A.) to the solution (arrowheads in Fig. 5A). Those acted as 'fracture-aids', giving good fractured specimens. In cryo-SEM imaging, the CNT arrangement within the solution was exposed by controlled e-beam etching of uncoated cryo-specimen areas, leaving signs of local radiation damage (black arrowhead in Fig. 5B). The relatively low viscosity of studied solution in biphasic region enabled us to prepare thin enough films for cryo-TEM imaging (Fig. 5C). The arrangement of the CNTs in the biphasic region, as observed by cryo-SEM (Figs. 5A,B), is consistent with our cryo-TEM data. A white arrow in Figure 5(C) points to a thick ($\sim$130 nm) bundle formed by merging thinner ones. The advantage of cryo-SEM over the cryo-TEM is its ability to image the spatial arrangement of CNT domains in both isotropic and nematic phases.

We also characterized a fully developed liquid crystalline phase by cryo-SEM. This phase is used as 'dope' for fibre spinning (Behabtu *et al.*, 2008; Davis *et al.*, 2009; Behabtu *et al.*, 2013). Figure 6 shows the liquid crystal domains formed by CCNI XBC (mostly double walled with $L/D \approx 3660$) and by the HiPco (SWNT with $L/D \approx 150$–2000) in CSA.

The two solutions have different viscosity and CNT stiffness because of the very different nanotube nature. The main differences are in aspect ratio (Bengio *et al.*, 2014), which leads to fully LC phase formation in CCNI XBC solution at much lower concentrations as compared to HiPco (Davis *et al.*, 2004; Parra-Vasquez *et al.*, 2010). Moreover, cryo-SEM micrographs indicate very different arrangement of these nanotubes at the nanoscale. The longer CNTs form elongated aligned domains with high degree of order along the CNT long axis, whereas the shorter CNTs form shorter, more disordered liquid crystalline bundles. We observed reduced or no specimen charging while imaging longer CNT at higher concentration, which implies CNT continuity in the bulk, leading to improved electron conductivity.

The judicious application of our newly developed cryo-EM methodology has allowed us to follow, on the nanoscopic scale, the process of CNT dissolution in CSA, the assembly of CNTs into aligned domains and finally the formation of a liquid crystalline nematic phase. Full analysis of physical chemistry of the process will be discussed in a forthcoming paper (Kleinerman, in preparation).

Conclusions

We have modified the cryo-TEM methodology, starting from cryo-specimen preparation, through imaging, and finally with micrograph interpretation, to allow us analyse the nanostructures formed by CNTs and graphene in their only true solvent, CSA. We also modified cryo-SEM to allow us prepare thermally-fixed specimens of viscoelastic solutions of CNTs in CSA, in which the nanostructures are fully preserved. While applying this new methodology, we have studied the process of electron-beam interaction with CSA based specimens, in imaging and electron-beam radiation damage.

The application of the combined methodologies of cryo-TEM and cryo-SEM has provided a wealth of new data, elucidating nanostructure and nanostructure development in the dissolution and self-assembly of CNTs in CSA. This methodology could be applied for the nanoscopic electron imaging of many other sensitive liquid or semiliquid systems.

Acknowledgements

We gratefully acknowledge useful discussions with Mr. L. Issman, and technical support of B. Shdemati.

Funding source: This work was funded by AFOSR grants FA9550-06-1-0207 and FA9550-09-1-0590, AFRL agreements FA8650-07-2-5061 and 07-S568-0042-01-C1, the Robert A. Welch Foundation (grant C-1668), the Evans-Attwell Welch Postdoctoral Fellowship, the United States-Israel Binational Science Foundation and Teijin Aramid. Cryo-TEM and cryo-SEM imaging was performed at the Technion Laboratory for Electron Microscopy of Soft Matter, supported by the Technion Russell Berrie Nanotechnology Institute.

References

Bang J., Jain S., Li Z., Lodge T.P., Pedersen J.S., Kesselman E. & Talmon Y. (2006) Sphere, cylinder, and vesicle nanoaggregates in poly(styrene-b-isoprene) diblock copolymer solutions. *Macromolecules* **39**, 1199–1208.

Behabtu N. (2012) Dissolution, processing and fluid structure of graphene and carbon nanotube in superacids: The route toward high performance multifunctional materials. PhD Thesis, Rice University.

Behabtu N., Lomeda J.R., Green M.J., *et al.* (2010) Spontaneous high-concentration dispersions and liquid crystals of graphene. *Nat. Nanotechnol.* **5**, 406–411.

Behabtu N., Young C.C., Tsentalovich D.E. *et al.* (2013) Strong, light, multifunctional fibers of carbon nanotubes with ultrahigh conductivity. *Science* **339**, 182–186.

Behabtu N., Green M.J. & Pasquali M. (2008) Carbon nanotube-based neat fibers. *Nano Today* **3**, 24–34.

Bekou S. & Mattia D. (2011) Wetting of nanotubes. *Curr. Opin. Colloid Interface Sci.* **16**, 259–265.

Bellare J.R., Davis H.T., Scriven L.E. & Talmon Y. (1988) Controlled environment vitrification system: an improved sample preparation technique. *J. Electron Microsci. Tech.* **10**, 87–111.

Bengio, E.A., Tsentalovich, D.E., Behabtu, N., Kleinerman, O., Kesselman, E., Schmidt, J., Talmon, Y. & Pasquali, M. (2014). Statistical length measurement method by direct imaging of carbon nanotubes. *ACS Appl. Mater. Interfaces*, **6**(9), 6139–6146.

Davis V.A., Ericson L.M., Parra-Vasquez A.N.G., *et al.* (2004) Phase behavior and rheology of SWNTs in superacids. *Macromolecules* **37**, 154–160.

Davis V.A., Parra-Vasquez A.N.G., Green M.J., *et al.* (2009) True solutions of single-walled carbon nanotubes for assembly into macroscopic materials. *Nat. Nanotechnol.* **4**, 830–834.

Dudkiewicz A., Tiede K., Loeschner K., *et al.* (2011) Characterization of nanomaterials in food by electron microscopy. *TrAC Trends Anal. Chem.* **30**, 28–43.

Egerton R. (2005) *Physical Principles of Electron Microscopy: An Introduction to TEM, SEM, and AEM*. Springer, New York.

Flory P.J. (1956) Phase equilibria in solutions of rod-like particles. *Proc. R. Soc. Lond. Ser. A, Math. Phys. Sci.* **234**, 73–89.

Flory P.J. & Abe A. (1978) Statistical thermodynamics of mixtures of rod-like particles, Part 1: Theory for polydisperse systems. *Macromolecules* **11**, 1119–1122.

Frederik, P.M. & Hubert, D.H.W. (2005). Cryoelectron microscopy of liposomes. *Methods Enzymol.* **391**, 431–448.

Friedrich H., Frederik P.M., de With G. & Sommerdijk N. (2010) Imaging of self-assembled structures: interpretation of TEM and cryo-TEM images. *Angewandte Chemie International Edition* **49**, 36–44.

Gogotsi Y., Naguib N. & Libera J.A. (2002) In situ chemical experiments in carbon nanotubes. *Chem. Phys. Lett.* **365**, 354–360.

Goldstein J., Newbury D.E., Joy D.C., *et al.* (2003) *Scanning Electron Microscopy and X-Ray Microanalysis*, 3rd edn. Springer, New York.

Green M.J., Behabtu N., Pasquali M. & Adams W.W. (2009a) Nanotubes as polymers. *Polymer* **50**, 4979-97.

Green M.J., Parra-Vasquez A., Behabtu N. & Pasquali M. (2009b) Modeling the phase behavior of polydisperse rigid rods with attractive interactions with applications to single-walled carbon nanotubes in superacids. *J. Chem. Phys.* **131**(8), 084901–10.

Green M.J., Young C.C., Parra-Vasquez A.N.G., *et al.* (2011) Direct imaging of carbon nanotubes spontaneously filled with solvent. *Chem. Commun.* **47**, 1228–1230.

Henriksen T. & Jones W.B.G. (1971) ESR studies of the mechanisms for radical formation in irradiated frozen sulfuric acid solutions of thymine. *Radiat. Res.* **45**, 420–33.

Hisada A., Yoshida T., Kubota S., Nishizawa N.K. & Furuya M. (2001) Technical advance: an automated device for cryo-fixation of specimens of electron microscopy using liquid helium. *Plant Cell Physiol.* **42**, 885–893.

Issman L. & Talmon Y. (2012) Cryo-SEM specimen preparation under controlled temperature and concentration conditions. *J. Microsc.* **246**, 60–69.

Jaksch, H., Steigerwald, M., Drexel, V. & Bihr, H. (2003). New detection principles and developments on the GEMINI SUPRA FE-SEM. *Microsc. Microanal.* **9**, 106–107.

Kesselman E., Talmon Y., Bang J., Abbas S., Li Z. & Lodge T.P. (2005) Cryogenic transmission electron microscopy imaging of vesicles formed by a polystyrene–polyisoprene diblock copolymer. *Macromolecules* **38**, 6779–6781.

Kleinerman, O. Liquid crystalline development in CNT/superacid solutions by cryogenic electron microscopy. In Preparation.

Knoll G., Oebel G. & Plattner H. (1982) A simple sandwich-cryogen-jet procedure with high cooling rates for cryofixation of biological materials in the native state. *Protoplasma* **111**, 161–176.

Larson R.G. (1999) *The Structure and Rheology of Complex Fluids*. Oxford University Press, New York.

Moor H. & Riehle U. (1968) Snap-freezing under high pressure: a new fixation technique for freeze-etching. *In Proc. 4th European Eur. Reg. Conf. of Electron Microscopy* **2**, 33–34.

Moor H., Kistler J. & Muller M. (1976) Freezing in a propane jet. *Experientia* **32**, 805.

Mortensen K. & Talmon Y. (1995) Cryo-TEM and SANS microstructural study of pluronic polymer solutions. *Macromolecules* **28**, 8829–8834.

Mueller M., Meister N. & Moor H. (1980) Freezing in a propane jet and its application in freeze-fracturing. *Mikroskopie* **36**, 129–140.

Omer L., Ruthstein S., Goldfarb D. & Talmon Y. (2009) High-resolution cryogenic-electron microscopy reveals details of a hexagonal-to-bicontinuous cubic phase transition in mesoporous silica synthesis. *J. Am. Chem. Soc.* **131**, 12466–12473.

Onsager L. (1949) The effects of shape on the interaction of colloidal particles. *Ann. N. Y. Acad. Sci.* **51**, 627–659.

Parra-Vasquez A., Behabtu N., Green M.J., *et al.* (2010) Spontaneous dissolution of ultralong single-and multiwalled carbon nanotubes. *ACS Nano* **4**, 3969–3978.

Pint C.L., Nicholas N., Pheasant S.T., *et al.* (2008) Temperature and gas pressure effects in vertically aligned carbon nanotube growth from Fe-Mo catalyst. *J. Phys. Chem. C* **112**, 14041–14051.

Plies E. (1994) Electron optics of low-voltage electron beam testing and inspection, Part IV: Coulomb interaction and electrostatic charging. *Adv. Opt. Electr. Microsc.* **13**, 216.

Pohl D. & Jaksch H. (1995) Progress in scanning secondary electron microscopy. *Bundesanstalt für Materialforschung und-Prüfung* **37**, 412–415.

Ramesh S., Ericson L.M., Davis V.A., *et al.* (2004) Dissolution of pristine single walled carbon nanotubes in superacids by direct protonation. *J. Phys. Chem. B* **108**, 8794–8798.

Siegel D.P., Green W.J. & Talmon Y. (1994) The mechanism of lamellar-to-inverted hexagonal phase transitions: a study using temperature-jump cryo-electron microscopy. *Biophys. J.* **66**, 402–414.

Steere, R.L. (1957) Electron microscopy of structural detail in frozen biological specimens. *J. Biophys. Biochem. Cytol.* **3**, 45–60.

Talmon Y. (2007) Seeing giant micelles by cryogenic-temperature transmission electron microscopy (cryo-TEM). *Giant Micelles: Properties and Applications* (ed. by R. Zana & E.W. Kaler), pp. 163–178. CRC Press, Boca Raton, FL.

Talmon Y., Adrian M. & Dubochet J. (1986) Electron beam radiation damage to organic inclusions in vitreous, cubic, and hexagonal ice. *J. Microsc.* **141**, 375–384.

Wepf R., Richter T., Sattler M. & Kaech A. (2004) Improvements for HR- and Cryo-SEM by the VCT 100 high-vacuum cryo transfer system and SEM cooling stage. *Microsc. Microanal.* **10**, 970–971.

Yan Y., Hoffmann H., Makarsky A., Richter W. & Talmon Y. (2007) Swelling of Lα-phases by matching the refractive index of the water-glycerol mixed solvent and that of the bilayers in the block copolymer system of (EO)15-(PDMS)15-(EO)15. *J. Phys. Chem. B* **111**, 6374–6382.